



Coronal Dimmings Associated with Coronal Mass Ejections on the Solar Limb

Galina Chikunova¹ , Karin Dissauer^{2,3} , Tatiana Podladchikova¹ , and Astrid M. Veronig^{3,4}

¹ Skolkovo Institute of Science and Technology, Bolshoy Boulevard 30, bld. 1, Moscow 121205, Russia; galina.chikunova@skoltech.ru

² NorthWest Research Associates, 3380 Mitchell Lane, Boulder, CO 80301, USA

³ Institute of Physics, University of Graz, Universitätsplatz 5, A-8010 Graz, Austria

⁴ Kanzelhöhe Observatory for Solar and Environmental Research, University of Graz, Kanzelhöhe 19, A-9521 Treffen, Austria

Received 2019 December 21; revised 2020 May 2; accepted 2020 May 5; published 2020 June 9

Abstract

We present a statistical analysis of 43 coronal dimming events associated with Earth-directed coronal mass ejections (CMEs) that occurred during the period of quasi-quadrature of the Solar Dynamics Observatory (SDO) and Solar Terrestrial Relations Observatory (STEREO) satellites. We studied coronal dimmings that were observed above the limb by STEREO Extreme Ultraviolet Imager and compared their properties with the mass and speed of the associated CMEs. The unique position of the satellites allowed us to compare our findings with the results from Dissauer et al., who studied the same events observed against the solar disk by the SDO Atmospheric Imaging Assembly. Such statistics is done for the first time and **confirms the relation of coronal dimmings and CME parameters for the off-limb viewpoint**. The observations of dimming regions from different lines of sight reveal a similar decrease in the total extreme ultraviolet intensity ($c = 0.60 \pm 0.14$). We find that the (projected) dimming areas are typically larger for off-limb observations (mean value of $1.24 \pm 1.23 \times 10^{11} \text{ km}^2$ against $3.51 \pm 0.71 \times 10^{10} \text{ km}^2$ for on-disk), with a correlation of $c = 0.63 \pm 0.10$. This systematic difference can be explained by the (weaker) contributions to the dimming regions higher up in the corona that cannot be detected in the on-disk observations. The off-limb dimming areas and brightnesses show very strong correlations with the CME mass ($c = 0.82 \pm 0.06$ and 0.75 ± 0.08), whereas the dimming area and brightness change rate correlate with the CME speed ($c \sim 0.6$). Our findings suggest that coronal dimmings have the potential to provide early estimates of the mass and speed of Earth-directed CMEs, relevant for space weather forecasts, for satellite locations at both L1 and L5.

Unified Astronomy Thesaurus concepts: Solar coronal mass ejections (310); The Sun (1693); Active sun (18)

1. Introduction

Coronal mass ejections (CMEs) are the most energetic and powerful eruptive phenomena on the Sun and also the main drivers of space weather effects. Huge amounts of magnetized plasma are expelled from the Sun to interplanetary space with speeds in the range of some 100 to $>3000 \text{ km s}^{-1}$ (Gopalswamy et al. 2009; Webb & Howard 2012) and may interact with the Earth's magnetosphere and atmosphere to produce geomagnetic storms and affect human environment and technologies (Gosling 1993; Lanzerotti 2017; Knipp et al. 2018).

Ironically, Earth-directed CMEs are most difficult to measure using observations from instruments along the Sun–Earth line due to strong projection effects (Burkepile et al. 2004). In these cases, we mostly observe the CME's expansion motion and not its propagation toward Earth. In addition, their initiation and early acceleration are also difficult to observe, as these regions are blocked by the coronagraph's occulter disk. The operation of NASA's Solar Terrestrial Relations Observatory (STEREO) mission (Kaiser et al. 2008) with its unique capability of imaging the inner heliosphere from two different vantage points away from the Sun–Earth line has greatly improved our understanding of CME structure and evolution (Aschwanden et al. 2009; Rouillard 2011; Thernisien et al. 2011). Depending on the position on their orbits around the Sun, the STEREO satellites provide us with the capability to observe Earth-directed CMEs from the side, including observations of their initiation and early evolution above the limb in extreme ultraviolet (EUV) and coronagraph observations by the Extreme Ultraviolet Imager (EUVI) and COR instruments.

Coronal dimmings are transient regions of strongly reduced emission in soft X-ray (Hudson et al. 1996; Sterling & Hudson 1997) and EUV (Thompson et al. 1998; Zarro et al. 1999) wavelengths that occur in association with CMEs. In general, they are interpreted as density depletion caused by mass loss during the CME eruption (Webb et al. 2000). The loss of mass in coronal dimmings is also evidenced by spectroscopic studies that identified plasma outflows in coronal dimming regions (e.g., Harrison & Lyons 2000; Harra & Sterling 2001; Tian et al. 2012; Veronig et al. 2019). **In addition, differential emission measure (DEM) analysis of coronal dimmings showed that the impulsive decrease of emission in dimming regions stems mostly from a distinct drop in density (up to 70%), whereas the variations in plasma temperature are much smaller** (López et al. 2017; Vanninathan et al. 2018; Veronig et al. 2019). Coronal dimmings are also closely associated with large-scale coronal waves initiated by CMEs (e.g., Thompson et al. 1998; Dissauer et al. 2016; Veronig et al. 2018; Podladchikova et al. 2019). Thus, coronal dimmings contain important information on the early CME evolution, characteristic CME properties, and associated shock waves.

Different approaches have been developed and used for the extraction of coronal dimmings: thresholding pixel values from base-difference (BD) images in Bewsher et al. (2008) and Reinard & Biesecker (2008), applying techniques of producing minimum and maximum intensity maps in the NEMO algorithm by Podladchikova & Berghmans (2005) and its extension by Attrill & Wills-Davey (2009), using the thresholded intersection of running-difference and percentage

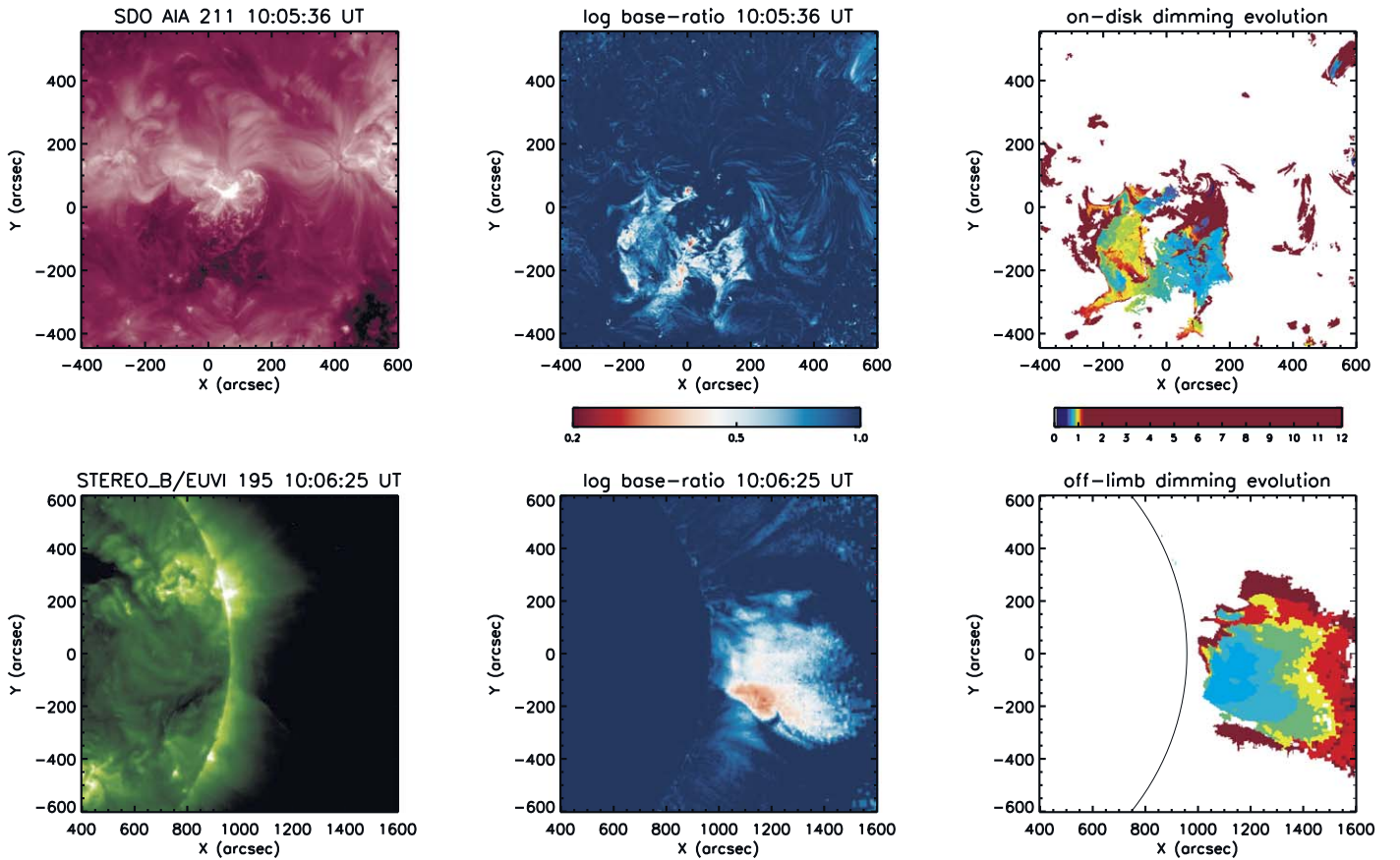


Figure 1. Illustration of the dimming evolution from two different viewpoints for the event of 2011 October 1. The top panels represent on-disk dimming observations: SDO/AIA 211 Å filtergram (left), LBR map (middle), and the timing map (right) that marks when each dimming pixel was detected for the first time (presented in hours after the flare onset). The bottom panels show the same for the off-limb dimming observations by STEREO-B/EUVI.

running-difference images in the Solar Demon algorithm by Kraaikamp & Verbeeck (2015), constructing Lambert projection maps from direct EUV data by the CoDiT software in Krista & Reinard (2012), and applying a thresholding-based algorithm using logarithmic base ratio (LBR) images in Dissauer et al. (2018a).

The automated algorithms allow one to process a large number of events and create a statistical basis of coronal dimmings and their associated CMEs. However, there exist only a few statistical studies of coronal dimmings (Bewsher et al. 2008; Reinard & Biesecker 2008; Aschwanden 2016; Mason et al. 2016; Krista & Reinard 2017). A thorough methodological approach and comprehensive statistical analysis of the characteristic properties of coronal dimmings and their relation to the decisive parameters of the associated CMEs and flares have recently been presented in a series of papers by Dissauer et al. (2018a, 2018b, 2019). In these studies, 62 dimming events were analyzed using multiple-viewpoint observations by the Solar Dynamics Observatory (SDO) and STEREO satellites in quasi-quadrature; coronal dimmings were observed on-disk by the SDO Atmospheric Imaging Assembly (AIA; Lemen et al. 2012), the related magnetic fluxes were obtained using the SDO Helioseismic and Magnetic Imager (HMI), and the kinematics and mass of the associated CME were observed in STEREO EUVI and COR data close to the limb, minimizing projection effects. These studies revealed that the CME mass shows high correlations with the dimming area and its total brightness and magnetic flux, whereas the maximal speed of the CME is strongly correlated with the corresponding

time derivatives (i.e., area growth rate, brightness change rate, and magnetic flux rate) with correlation coefficients in the range of $c \sim 0.6$ – 0.7 (Dissauer et al. 2018b, 2019).

In this paper, we study the same data set but extract the coronal dimming properties and their evolution from STEREO/EUVI, which observes the dimmings above the limb. This approach allows us for the first time to compare the results of on-disk and off-limb observations of coronal dimmings, as well as study how the viewing position affects the derived properties.

For illustration, we show Figure 1 as an example of the different appearance of the dimming event that occurred on 2011 October 1, observed on-disk by SDO/AIA (Dissauer et al. 2019) and off-limb by the STEREO-B satellite. We show the direct SDO/AIA 211 Å (top) and STEREO-B/EUVI 195 Å (bottom) images close to the time of maximal extent of the dimming, the corresponding LBR images, and the timing maps. The colors in the timing maps encode for each dimming pixel the time of its first detection.

2. Data and Data Reduction

In this study, we use data from NASA’s STEREO (Kaiser et al. 2008). The EUVI (Wuelser et al. 2004) of the STEREO/SECCHI instrument suite provide images of the Sun with a pixel scale of $1''.6$ through four EUV filters. We used filtergrams of the 195 Å passband with a cadence of 5 minutes (except for individual events, where it can vary from 1.5 to 10 minutes). According to Dissauer et al. (2018a) and Kraaikamp & Verbeeck (2015),

coronal dimmings are best observed in wavelengths sensitive to quiet Sun coronal temperatures (e.g., 195, 171, and 211 Å). We use the wavelength 195 Å because it has the highest cadence for STEREO/EUVI.

We study the time range between 2010 May and 2012 September when SDO was in quasi-quadrature with the STEREO-A and STEREO-B satellites, increasing their separation angle to the Sun–Earth line during this period from $\pm 75^\circ$ to $\pm 125^\circ$. We focus on 43 events in which coronal dimmings and their associated Earth-directed CMEs were observed off-limb by at least one of the two STEREO satellites. Thirty-nine of these events overlap with the event set from Dissauer et al. (2018b, 2019), who studied the same dimmings as observed on-disk by the AIA instrument on board NASA’s SDO satellite (Lemen et al. 2012). Four events were excluded in the Dissauer et al. (2018b, 2019) studies due to filament material that partially obscured the on-disk dimming detection. This was not the case for the STEREO off-limb observations; thus, they are included in the present work. However, for 23 events of the overall data set of 62 events, the off-limb dimming extraction was not possible due to only partial visibility of the dimmings by the STEREO satellites or the activity of multiple active regions at the same time. One event (2012 July 2) was excluded from the statistics due to its complexity (disappearance of transequatorial loops) revealed during the comparative analysis from the two viewpoints.

The kinematical CME parameters used for comparison with the derived dimming properties are from the STEREO/EUVI and COR measurements in Dissauer et al. (2019). The fastest event in the data set occurred on 2012 March 6 with a maximal velocity of $\sim 3700 \text{ km s}^{-1}$ and mass of $1.83 \times 10^{16} \text{ g}$. For the other events, the maximal velocities of the CMEs vary from 370 to 2000 km s^{-1} , and the values of CME masses lie between 2.03×10^{14} and $1.78 \times 10^{16} \text{ g}$.

For each event, we analyze a series of STEREO/EUVI images that begin 30 minutes before the associated flare and last for 12 hr in total. All EUVI images of the data set were checked for the exposure time, prepared with standard SolarSoft routines (`secchi_prep.pro`), and corrected for differential rotation (`drot_map.pro`). The images were cut automatically by half (either eastern or western hemisphere), depending on which satellite observed the event better, STEREO-A or STEREO-B.

3. Methods and Analysis

In this paper, we study the evolution of off-limb coronal dimmings and their corresponding CMEs. We derive characteristic dimming parameters, such as area, brightness, and duration, using observations where the coronal dimmings and the associated CME are observed off-limb by STEREO. The dimming segmentation algorithm is demonstrated for two example events that occurred on 2011 October 1 (event no. 19, impulsive M1.2 flare associated with an EUV wave) and 2012 March 6 (event no. 29, impulsive X5.4 flare associated with an EUV wave and a halo CME).

3.1. Dimming Extraction Algorithm

We identify the area and the brightness of the dimming regions observed off-limb by applying an automated detection technique based on thresholding and region growing. Usually, BD images are used for the recognition of dimmings (e.g., the

algorithms in Reinard & Biesecker 2008; Attrill & Wills-Davey 2009), which show absolute changes in intensity. However, some regions of coronal dimming represent only a slight decrease in intensity or may develop in the upper corona, where the density is lower. Therefore, such changes are difficult to identify by their absolute value compared to other differences in the coronal intensity.

In Dissauer et al. (2018a), the advantage of using LBR images has been discussed. This form of preprocessing the data is based on dividing each frame of the series by a pre-event image. Thus, these images reflect relative changes in logarithmic intensity, which for the off-limb dimmings also allow us to detect regions higher up in the corona. It is worth mentioning that the application of the logarithm to the ratio images is identical to the difference of the logarithmic images. However, the usage of the ratio also leads to more intensity fluctuations, especially in regions higher up in the corona. Thus, we combine both types of data preprocessing to reduce this noise in the extraction of the dimming regions while still being sensitive to also detecting smaller intensity changes due to dimmings. We use a region-growing algorithm (Podladchikova & Berghmans 2005), which examines neighboring pixels of initial seed points and determines whether the pixel neighbors should be added to the region or not. It is not possible to define the seed pixels in LBR data due to the noise in the upper corona. Therefore, we combine both BD and LBR data preprocessing: we use BD images for identification of the darkest pixels that will later form the seed pixels applied to the regions in the corresponding areas in LBR images. Since the seed pixels are generally not directly connected to the fluctuations identified higher up in the corona, this approach provides a robust means to detect and segment dimming regions above the limb for both strong and weak dimmings.

First, we threshold BD data by -1.0 DN and extract 30% of the darkest pixels from it. In this way, the number of pixels with an intensity drop of more than -1.0 DN form the array of seed pixels for the region-growing algorithm (see Figure 3(d)). We use the darkest pixels in the BD data because this criterion is independent of a fixed threshold and is therefore not affected by the changes in the mean intensity in the overall corona over time.

In the next step, we select the thresholding level for LBR data: all pixels with an LBR intensity decrease below a value of -0.19 (which corresponds to a relative decrease by approximately 35% in linear space) are identified as dimming pixels (see Figure 3(e)). Our threshold was found empirically from the histograms by qualitatively checking different images during different development states of the dimming for several events (see also Dissauer et al. 2018a, Figure 2). The thresholding level appeared to be the same as found in Dissauer et al. (2018a) for SDO/AIA data, as it performed well to separate the dimming pixel distribution from random noise within the majority of histograms investigated for the STEREO/EUVI data. In Figure 2, we show for two sample events the intensity distribution of the LBR images for two different time steps, one before and one during the dimming. The state before the dimming formation is presented as a black histogram and shows a small variance in values; the dimming state at the time close to its maximal extent is presented as green histogram and reveals a systematic shift to negative intensity values, indicating the dimming pixels. The chosen thresholding level of -0.19 (blue vertical line) provides a basic, first-level

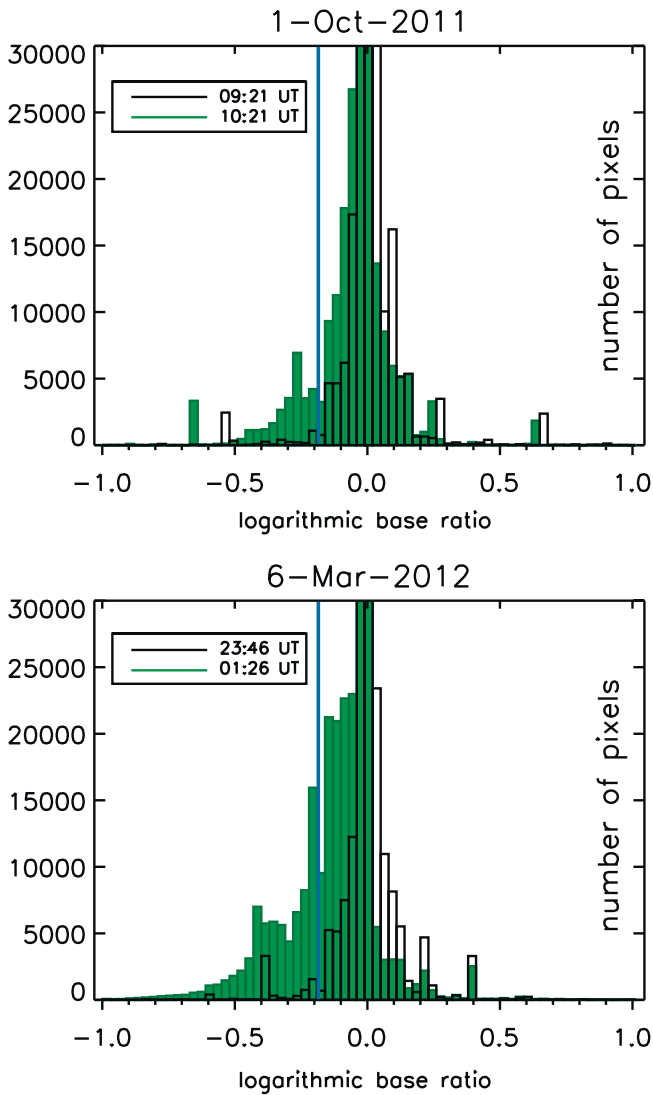


Figure 2. Intensity distributions of LBR images for dimming events that occurred on 2011 October 1 (top) and 2012 March 6 (bottom). The black histogram is calculated from an image during a pre-event time step (i.e., nondimming state), and the green histogram is from an image during the time of maximal extent of the dimming. Note the shift toward negative intensity values for the distribution during the dimming state (green). The value used for first-level thresholding is shown by the blue vertical line.

separation of the nondimming fluctuations in the image and the dimming pixels.

In order to reduce noise and the number of misidentified pixels, morphological operators (with a kernel of 3×3 pixels) are used to smooth the extracted regions and remove small-scale features. It also helps in situations where gaps need to be filled in order to let seed pixels grow to more distant dimming parts. Finally, only pixels of LBR data that represent direct neighbors of the seed pixels in BD data create the dimming region (see Figure 3(f)) and are subsequently used to extract the properties (area, intensity) of the dimming regions.

In Figure 3, we illustrate all of the major steps of the dimming detection algorithm. The top panels show the original data (a), the BD image (b), and the LBR image (c). The masks of the extracted regions for each step are shown in the bottom panels: the darkest pixels derived from the BD image (d), which are used as the seed pixels in the thresholded LBR data (e) by applying the region-growing algorithm to form the final

dimming region (f). As can be noticed, the noise in the LBR data is mostly present in regions higher up in the corona and does not overlap with the noise of the BD data in the low corona. Thus, the chosen approach combining the two types of data is effective for the dimming extraction above the solar limb.

3.2. Characteristic Coronal Dimming Parameters

The set of parameters that we derive to characterize coronal dimmings and their evolution is extracted by the same approach as described in Dissauer et al. (2018b). We derive instantaneous and cumulative dimming areas from LBR data, instantaneous and cumulative brightness from both BD and LBR data, and their derivatives and the duration of the impulsive phase of the dimming, i.e., the time range when most of the dimming region develops.

Instantaneous dimming masks are binary masks representing all dimming pixels detected at each time step. Cumulative dimming pixel masks are calculated by combining all pixels that were identified as dimming pixels up to a specific time. The choice of the approach for defining the dimming region influences the information we can extract from the evolution of the derived parameters. Cumulative masks allow us to study the full extent of the total dimming region over time. Figures 4 and 5 show the evolution of the cumulative dimming masks for the example events (2011 October 1 and 2012 March 6, respectively). The left and middle panels show snapshots of the original and LBR STEREO/EUVI images. The corresponding dimming cumulative masks, extracted by our algorithm, are presented in the right panels. Green pixels show the newly detected dimming regions, while gray pixels represent all pixels that were extracted as part of the dimming region during previous time steps.

By using the extracted masks, the evolution of coronal dimming regions is studied by the instantaneous and cumulative areas: the instantaneous area $A_{in}(t_i)$ represents the number of pixels identified as dimming pixels at a certain time step t_i , and the cumulative area $A_{cu}(t_i)$ is determined by combining the number of all dimming pixels detected up to time t_i . The corresponding area growth rate $dA/dt(t_i)$ characterizes how fast the dimming is developing; it is calculated as the corresponding time derivative of $A_{in}(t)$ or $A_{cu}(t)$ (see also Dissauer et al. 2018a). The time evolution of these quantities allows us to study the dynamic evolution of the dimming region and determine its impulsive phase.

The difference between instantaneous and cumulative masks, leading to a difference between the area parameters, can be seen in Figure 6, which shows the development of the coronal dimming region for the event that occurred on 2012 March 6. The start of the dimming impulsive phase (left), the time step of the maximum area growth rate (middle), and a time step 20 minutes after the end of the impulsive phase (right) are presented by the original STEREO/EUVI 195 Å filtergrams (first row), LBR data (second row), and instantaneous (third row) and cumulative (fourth row) masks. While the evolution of the event is rapid, the masks differ from each other mostly after the end of the impulsive phase of the dimming, when the cumulative area still contains the dimming parts extracted previously, although it is already shrinking.

The total instantaneous brightness $I_{in}(t_i)$ of the dimming region at a certain time step is calculated as the sum of all dimming pixel intensities at the time t_i . Instantaneous

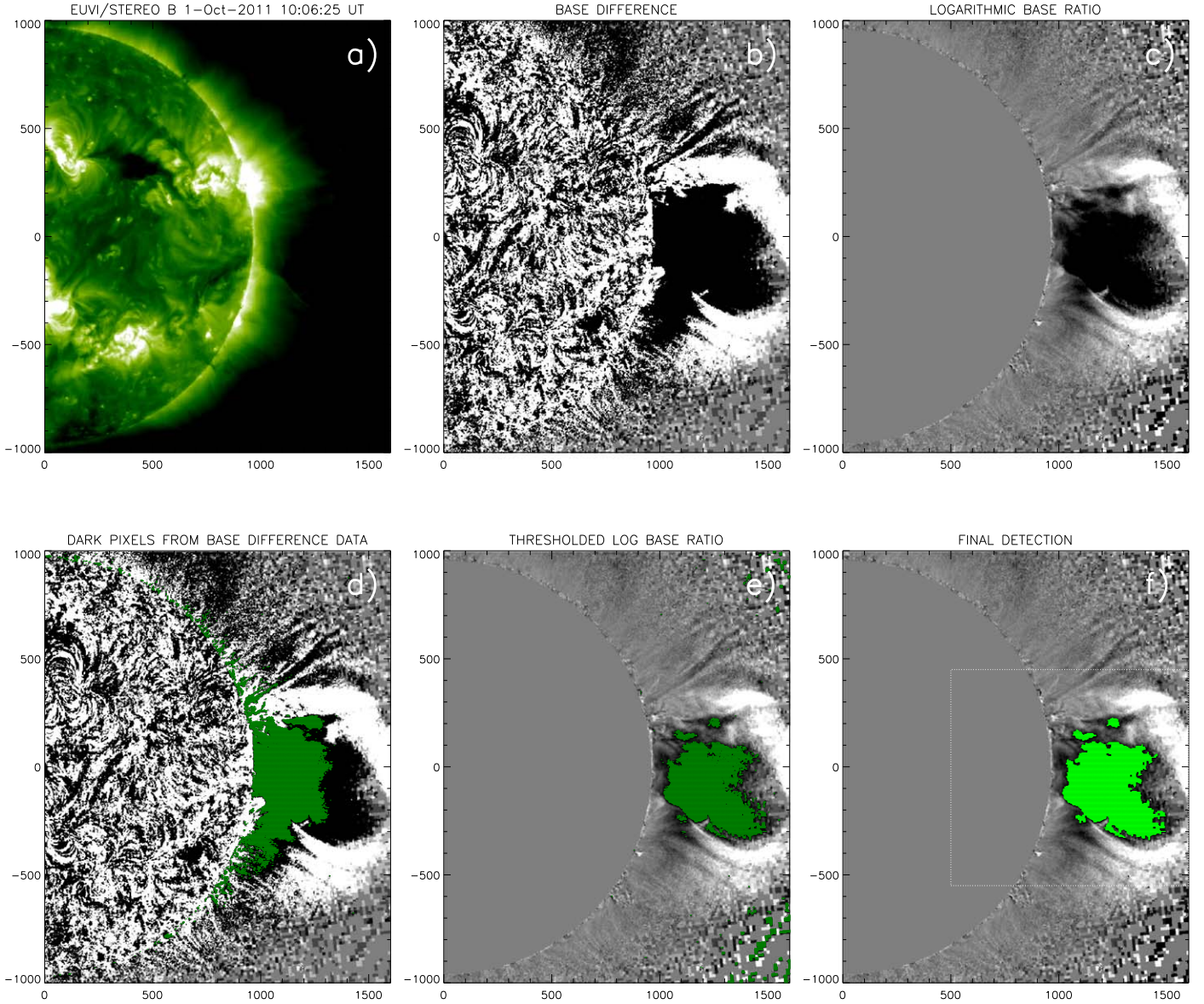


Figure 3. Dimming detection for the event on 2011 October 1. The top panels present original EUVI/STEREO 195 Å filtergrams (a) together with BD (b) and LBR (c) data. The bottom panels highlight pixels identified during the different steps of the detection: the darkest pixels extracted from BD data (d), LBR data thresholded by level -0.19 (e), and the final dimming region segmented for this time step in LBR data (f). The coordinates are given in arcseconds from Sun center. The white rectangle in the last panel indicates the region shown in Figure 4.

brightness values depend on both the area and the intensity of the pixels. In addition, to have a parameter that does not depend on the changing dimming area, we use one constant area A , representing the cumulative dimming mask at the end of the impulsive dimming evolution. The sum of pixel intensities from this area at each time step t_i determines the cumulative brightness $I_{cu}(t_i)$. This parameter shows the intensity of all dimming pixels that were detected until the end time of the impulsive dimming evolution t_{end} ; thus, it varies only because of the changes in the intensity of the dimming pixels, and it does not depend on changes in the dimming area over time. The brightness change rate is given by the corresponding time derivative. Also, we define the mean intensity of the dimming region $\bar{I}_{in}(t_i)$ by dividing the total instantaneous dimming brightness $I_{in}(t_i)$ by the instantaneous dimming area $A_{in}(t_i)$ at time t_i and $\bar{I}_{cu}(t_i)$ by dividing the total cumulative brightness $I_{cu}(t_i)$ by the constant dimming area A .

Coronal dimmings start to develop cotemporal with the early evolution of CMEs and may remain for several hours after they were formed (e.g., Dissauer et al. 2018b; Vanninathan et al. 2018). We study the impulsive phase of the coronal dimming evolution, defined by the area growth rate profile dA/dt . Following the definition in Dissauer et al. (2018a, 2018b), we define the start of the impulsive phase t_{start} as the local minimum that occurs closest in time before the highest peak of dA/dt . The end of the impulsive phase t_{end} is defined as the time step when the value of the area growth rate falls below 15% of its maximum:

$$\dot{A}(t) \leq 0.15 \cdot \dot{A}_{max}. \quad (1)$$

Thus, the duration of the impulsive phase of the coronal dimming can be estimated as the difference between t_{end} and t_{start} (note that the time cadence of STEREO/EUVI images is

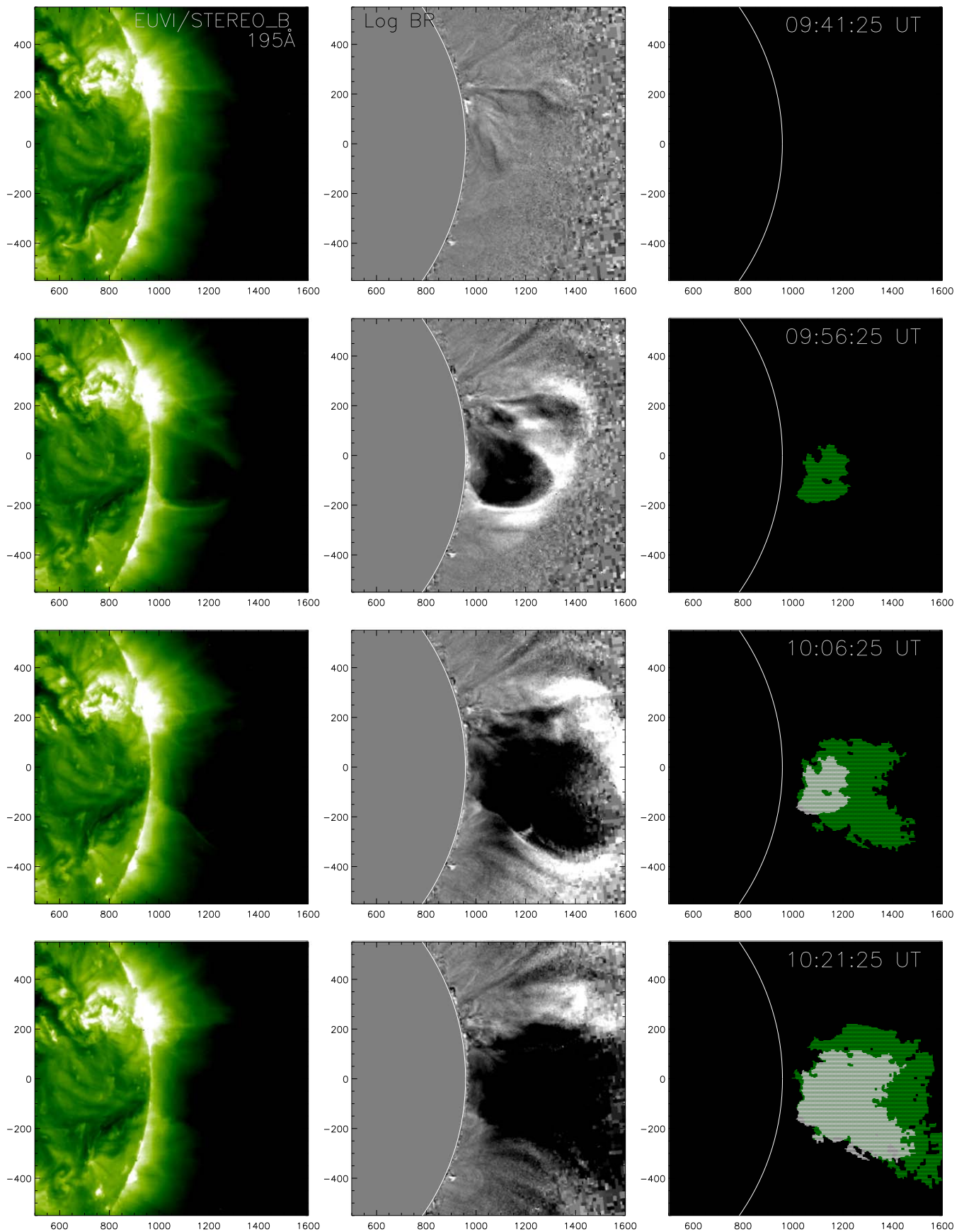


Figure 4. Coronal dimming evolution for the 2011 October 1 event. From left to right: direct EUVI/STEREO-B filtergrams, LBR images, and cumulative dimming pixel masks. All maps are zoomed to the region of the dimming location marked in Figure 3. In the right panels, the green pixels on top of the cumulative dimming pixel masks (gray regions) represent all newly detected pixels compared to the previously shown time step. The white contour in the middle and right panels indicates the solar limb. The time of each detection is given in the top right corner of each panel. The values of the axes are given in arcseconds.

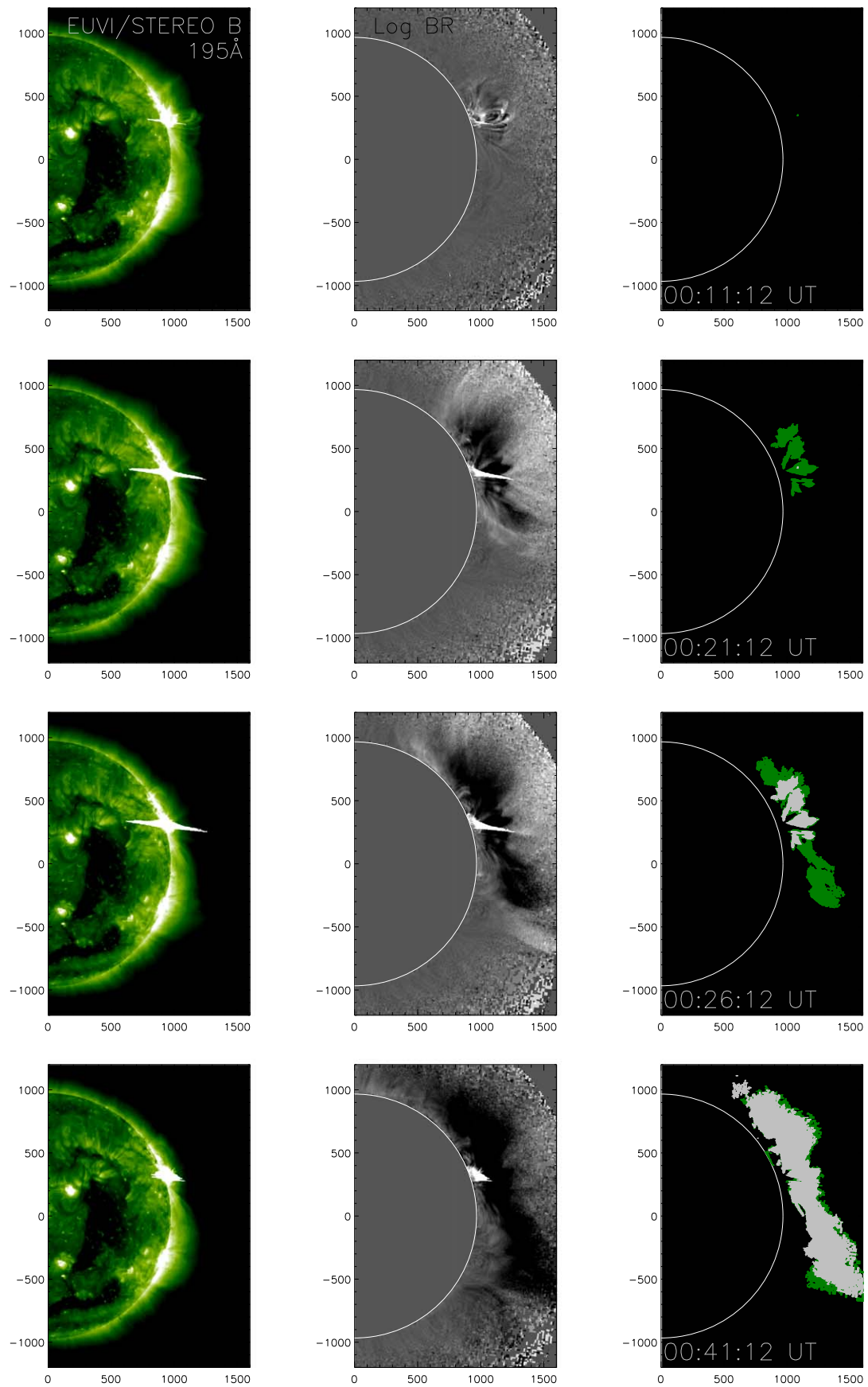


Figure 5. Same as Figure 4, but for the 2012 March 6 event.

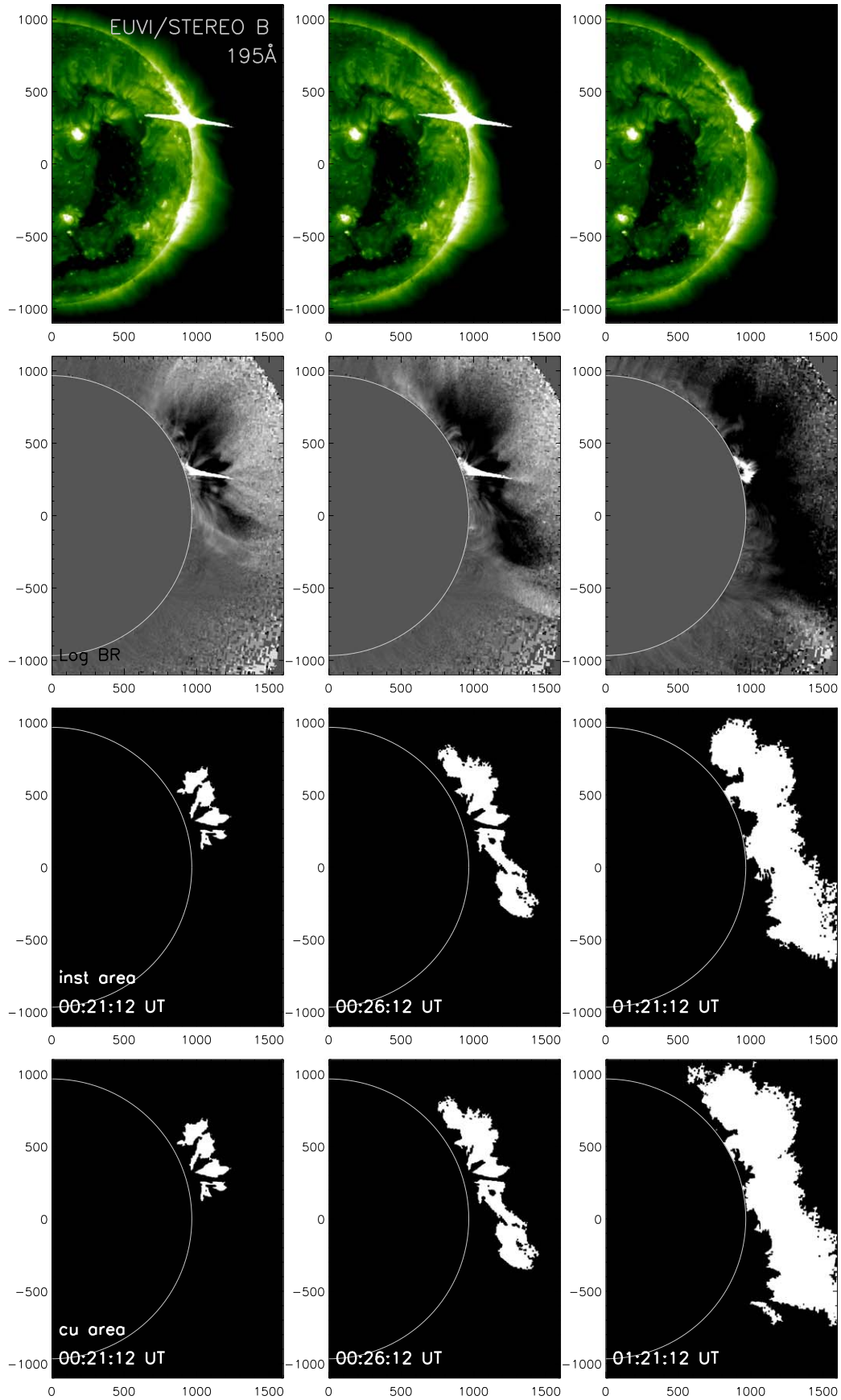


Figure 6. Example of instantaneous and cumulative dimming masks for the 2012 March 6 event. The first row presents original STEREO-B/EUVI filtergrams, while the second row shows the corresponding LBR data. The third and fourth rows show instantaneous and cumulative dimming pixel masks, respectively. The snapshots shown correspond to the following phases during the dimming evolution: close to the start of the impulsive phase (left), the moment of the maximum area growth rate (middle), and 20 minutes after the end of the impulsive phase (right). The white contour indicates the solar limb. The values of the axes are given in arcseconds.

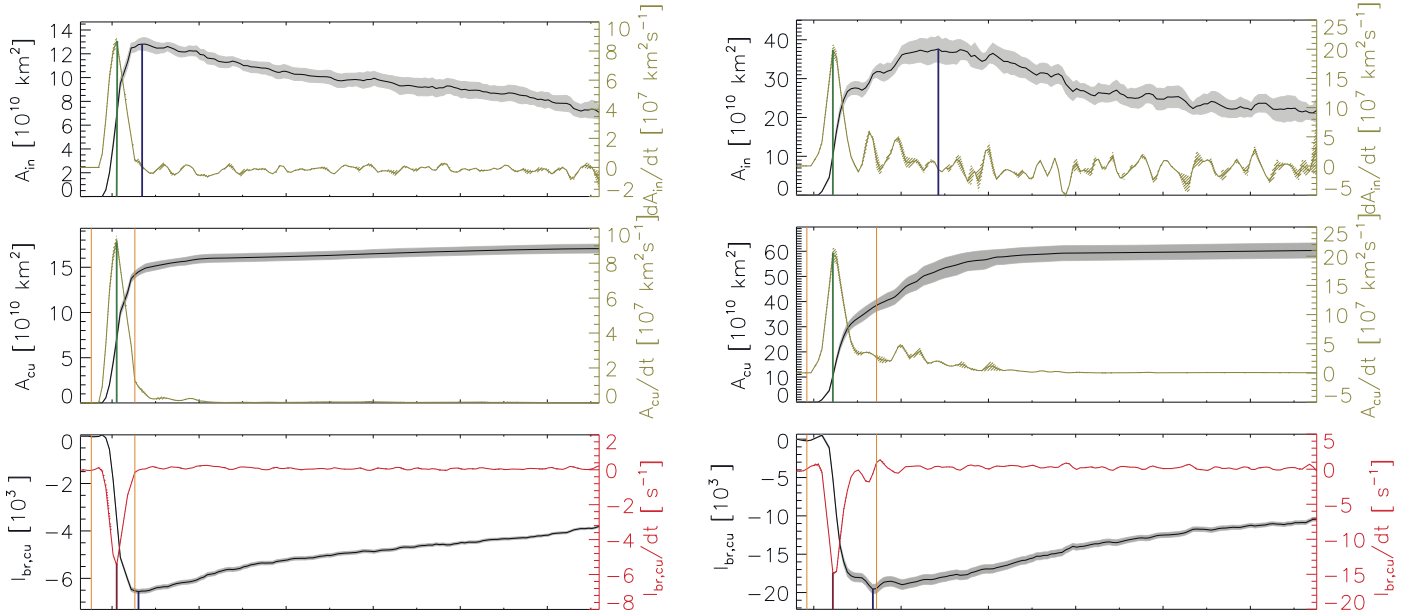


Figure 7. Time evolution of the dimming parameters for the events that occurred on 2011 October 1 (left) and 2012 March 6 (right): (top) instantaneous area A_{in} (black) and its growth rate (green), (middle) cumulative area A_{cu} (black) and its growth rate (green), and (bottom) cumulative brightness from LBR maps $I_{br,cu}$ (black) and its change rates (red). The light gray bands show the uncertainty ranges for each parameter (1σ). Orange boundaries represent the start and end times of the impulsive phase, green vertical lines show the maximum of the area growth rate, blue lines show the maximum of the instantaneous area or the minimum of the brightness, and dark red line marks the minimum of the brightness change rate.

5 minutes, which restricts the accuracy of the calculation of the duration parameter):

$$t_{dur} = t_{end} - t_{start}. \quad (2)$$

To estimate the uncertainty of the extracted parameter values caused by using a specific threshold for segmenting the dimming regions, we applied a $\pm 5\%$ change to the logarithmic threshold level of -0.19 and then calculated the mean value and standard deviation σ for all of the dimming parameters (see Figure 7).

4. Results

We study a set of 43 coronal dimming events that are observed above the limb by the STEREO-A or STEREO-B EUVI instruments in the 195 \AA passband (see Table 1). These events have been observed during a period where the STEREO satellites were in quasi-quadrature with spacecraft located along the Sun–Earth line, and the same dimming events have been studied in observations against the solar disk by the SDO/AIA in Dissauer et al. (2018b, 2019). For 37 events in our list, we also have the CME mass, and for 27 events, we have the CME maximum velocity derived from STEREO/EUVI and COR data in Dissauer et al. (2019). In Section 4.1 we present the temporal evolution of the dimming characteristics and their distribution. In Section 4.2 we relate our findings for the off-limb dimmings observed by EUVI to the results obtained for the corresponding on-disk dimming events observed by SDO/AIA from Dissauer et al. (2018b). In Section 4.3 we study the correlations of the decisive parameters describing off-limb coronal dimmings that we derived with the speed and mass of their associated CMEs.

All the plots presented in the following sections show the mean values of the derived parameters, while the error bars represent the 1σ standard deviation. The plots are presented in logarithmic space. The Pearson correlation coefficient c and the

linear regression fits shown are also derived in logarithmic space, i.e., $\log(y) = d + k \cdot \log(x)$. The values of the obtained correlation and fit parameters are annotated in each of the scatter plots shown. To obtain the mean and the standard deviation of c , we apply a bootstrap method (Wall & Jenkins 2012): we select random data pairs with replacements and repeat the procedures, calculating the Pearson coefficient 10,000 times. In the same way as Kazachenko et al. (2017) and Dissauer et al. (2018b), we classify the level of correlation as $c = [0.2, 0.4]$: weak; $c = [0.4, 0.6]$: moderate; $c = [0.6, 0.8]$: strong; and $c = [0.8, 1.0]$: very strong.

4.1. Evolution of the Dimming Parameters and Their Distribution

Figure 7 shows the time evolution of the coronal dimming parameters for two example events. The top and middle panels show the instantaneous A_{in} and cumulative A_{cu} area (black), respectively, together with the corresponding area growth rates (green). The bottom panels show the total cumulative brightness $I_{br,cu}$ and its change rate (red). We note that the evolution of the total brightness is representative for the different brightness definitions, as they all are similar to each other, reaching their minimum at the same time (only six events from our data set reveal a significant difference in time of the minimum of instantaneous and cumulative brightness; one of them is the example event of 2012 March 6). The gray shaded bands represent the 1σ range. Vertical lines indicate the start and end times of the dimming impulsive phase (orange), the maximum of the area growth rate (green), the maximum of the instantaneous area and the minimum of the brightness (blue), and the brightness change rate (red). In each event, the intensity decreases rapidly when the dimming area expands. The same tendency can be seen for the cumulative parameters, indicating that at this time, the dimming regions become not only bigger but also darker.

Table 1
Characteristic Dimming and CME Parameters

No.	Date	Sc.	A_{\max} (km ²) (10 ¹⁰)	A (km ²) (10 ¹⁰)	\dot{A} (km ² s ⁻¹) (10 ⁷)	$I_{br, cu}$ (10 ³)	$I_{br, in}$ (10 ³)	$I_{bd, cu}$ (DN) (10 ⁵)	$I_{bd, in}$ (DN) (10 ⁵)	$\bar{I}_{br, in}$	$\dot{I}_{br, in}$ (s ⁻¹)	t_{dur} (minutes)	m_{CME} (g) (10 ¹⁵)	v_{\max} (km s ⁻¹) (10 ³)
1	2010 Jul 16	B	0.76	1.50	0.40	-0.38	-0.28	-0.57	-1.20	-0.18	-0.11	120	...	0.37
2	2010 Aug 1	A	22.68	29.81	11.73	-16.93	-15.22	-5.83	-6.00	-0.33	-6.89	100	4.05	1.26
3	2010 Aug 7	A	8.79	10.56	6.30	-4.97	-4.50	-2.08	-1.84	-0.25	-2.84	55	6.69	0.96
4	2011 Feb 13	A	7.86	10.45	3.77	-4.26	-4.14	-4.20	-3.27	-0.26	-1.48	105	2.50	1.02
5	2011 Feb 14	A	0.48	0.70	0.27	-0.30	-0.29	-1.20	-1.51	-0.30	-0.07	65	0.47	...
6	2011 Feb 15	A	5.69	7.56	2.98	-3.52	-3.01	-3.93	-3.25	-0.26	-1.56	80	6.27	1.33
7	2011 Mar 7	B	1.54	2.19	0.80	-0.80	-0.64	-0.78	-0.40	-0.21	-0.30	90	4.34	1.10
8	2011 Jun 21	A	16.37	21.22	8.27	-13.61	-12.46	-14.45	-13.72	-0.38	-7.39	77	6.97	1.00
9	2011 Jul 11	A	9.52	8.83	5.71	-5.81	-6.22	-1.99	-3.56	-0.33	-3.19	50	1.48	0.53
10	2011 Aug 2	A	11.24	12.67	9.66	-8.23	-7.97	-4.15	-4.66	-0.36	-5.95	40	6.98	...
11	2011 Aug 3	A	18.14	22.68	6.62	-12.30	-11.08	-4.13	-4.80	-0.30	-3.11	105	7.69	1.61
*12	2011 Aug 4	A	13.27	21.67	12.71	-10.80	-8.35	-3.12	-2.23	-0.34	-6.16	55	6.77	...
13	2011 Sep 6	A	26.56	27.52	20.19	-17.70	-18.37	-7.00	-8.64	-0.34	-13.26	40	4.95	0.93
14	2011 Sep 6	A	36.88	41.07	24.92	-31.07	-30.38	-20.46	-20.11	-0.41	-21.43	70	10.85	1.15
*15	2011 Sep 7	A	20.76	26.91	16.00	-14.95	-12.89	-12.21	-11.39	-0.31	-9.66	55	5.35	...
16	2011 Sep 8	A	0.81	0.71	0.45	-0.26	-0.38	-0.46	-0.72	-0.23	-0.17	55	0.22	0.37
17	2011 Sep 27	B	0.92	1.00	0.61	-0.40	-0.39	-1.96	-1.73	-0.21	-0.23	65
18	2011 Sep 30	A	2.02	2.28	0.88	-1.15	-1.09	-2.59	-2.41	-0.27	-0.37	95
19	2011 Oct 1	B	12.81	14.17	9.32	-6.55	-6.24	-3.36	-3.18	-0.24	-4.22	60	...	0.57
20	2011 Oct 2	A	3.65	5.80	2.63	-2.46	-1.83	-3.05	-2.87	-0.25	-1.35	65	2.43	0.84
21	2011 Oct 2	A	1.61	1.91	1.06	-0.93	-0.86	-1.35	-1.28	-0.26	-0.55	70	1.73	0.63
22	2011 Nov 24	A	10.09	12.24	2.99	-6.61	-6.07	-13.87	-14.26	-0.30	-1.69	155	3.02	...
23	2011 Dec 22	A	3.81	4.55	2.79	-2.21	-1.99	-1.74	-1.70	-0.26	-1.34	55	2.37	...
24	2011 Dec 25	A	2.68	1.95	1.13	-1.60	-1.20	-2.62	-1.42	-0.22	-0.39	40
25	2011 Dec 25	A	5.73	7.01	7.03	-3.43	-2.98	-3.99	-3.81	-0.26	-3.36	40	5.90	...
26	2011 Dec 26	A	14.56	16.50	8.86	-8.46	-8.14	-3.46	-3.43	-0.28	-4.05	60	4.60	1.02
*27	2012 Jan 19	B	30.02	29.98	16.14	-17.50	-17.83	-5.64	-6.54	-0.30	-8.69	66	13.55	...
28	2012 Jan 23	A	12.59	16.87	12.26	-8.88	-7.84	-6.27	-5.38	-0.31	-6.70	50	12.45	1.99
29	2012 Mar 6	B	37.64	38.49	20.36	-19.57	-21.78	-11.71	-16.72	-0.29	-11.38	90	18.35	3.69
30	2012 Mar 9	B	7.25	8.71	6.85	-3.47	-3.13	-2.80	-2.49	-0.21	-2.92	30	7.02	1.25
31	2012 Mar 10	A	18.93	23.93	12.13	-15.84	-14.29	-9.96	-10.85	-0.38	-9.22	70	10.83	1.65
32	2012 Mar 14	A	5.64	5.73	3.61	-3.48	-3.51	-3.62	-3.62	-0.31	-2.16	50	3.41	...
33	2012 Mar 17	A	2.04	1.95	1.82	-1.20	-1.28	-1.15	-1.43	-0.31	-0.94	30	0.20	...
34	2012 Apr 5	A	11.56	15.17	9.15	-8.53	-7.97	-2.38	-2.10	-0.34	-4.42	50	5.95	...
35	2012 May 11	A	2.53	2.87	0.75	-1.48	-1.38	-1.57	-1.53	-0.27	-0.43	130	3.37	1.16
36	2012 Jun 3	B	12.32	11.30	10.46	-6.08	-6.98	-1.57	-2.39	-0.29	-5.26	35	3.68	...
37	2012 Jun 6	A	4.84	5.71	4.58	-2.61	-2.42	-0.96	-0.80	-0.25	-2.09	40	3.13	0.77
38	2012 Jun 14	A	10.80	12.59	7.23	-6.65	-6.36	-3.76	-4.02	-0.29	-3.71	65	7.76	1.44
39	2012 Jul 12	B	49.80	54.77	29.76	-34.76	-34.81	-7.31	-7.06	-0.35	-18.16	55	17.80	1.27
*40	2012 Aug 4	B	6.56	12.45	3.58	-3.81	-2.80	-4.70	-3.38	-0.21	-1.24	25	11.05	...
41	2012 Aug 15	A	1.10	2.04	1.38	-0.74	-0.49	-0.30	-0.15	-0.22	-0.43	50	1.03	0.60
42	2012 Sep 25	B	4.52	4.75	3.35	-1.57	-1.89	-0.73	-1.57	-0.21	-1.04	35	...	0.47
43	2012 Sep 27	A	8.88	12.21	7.47	-5.67	-4.70	-3.33	-2.71	-0.26	-4.00	80	9.37	1.50

Note. For each event, we list the STEREO satellite used for the analysis and the derived dimming characteristics: the dimming instantaneous area A_{\max} , cumulative area A , maximal cumulative area growth rate \dot{A} , total dimming brightness from LBR data (cumulative $I_{br, cu}$ and instantaneous $I_{br, in}$), total dimming brightness from BD data (cumulative $I_{bd, cu}$ and instantaneous $I_{bd, in}$), mean instantaneous brightness $\bar{I}_{br, in}$, brightness change rate $\dot{I}_{br, in}$, and duration of the impulsive phase of the dimming t_{dur} . The CME quantities are also given: the mass of the CME m_{CME} and the maximal speed of the CME v_{\max} . Events marked with an asterisk are not included in the on-disk dimming study by Dissauer et al. (2018b, 2019).

Studying the time evolution of the coronal dimming characteristics, we extract parameters for the statistics and comparison with the CME quantities. We define the dimming size A by the cumulative area at the end of the impulsive phase of the dimming t_{end} . The maximum of the instantaneous area A_{\max} is defined as the largest size of the dimming region during the 6 hr after the start of the impulsive phase. The area growth rate parameters are obtained by the maximum of the $dA_{cu}(t)/dt$ and $dA_{in}(t)/dt$ profiles, respectively.

Figure 8 compares the values of the parameters A_{\max} and A . The black line represents the linear regression fit to all data

points. The coefficients of the fitting line are presented in the bottom right corner ($k = 0.97$, $d = 0.41$). The corresponding correlation coefficient is given in the top left corner ($c = 0.99 \pm 0.01$). The high positive value of c and the slope of the fitting regression line $k \sim 1$ illustrate that the two different approaches for identifying the dimming area provide almost identical results.

We also extract the minimum of the total brightness for BD (instantaneous $I_{bd, in}$ and cumulative $I_{bd, cu}$) and LBR (instantaneous $I_{br, in}$ and cumulative $I_{br, cu}$) data. Because $I(t)$ usually reaches the minimum after the dimming impulsive phase, we

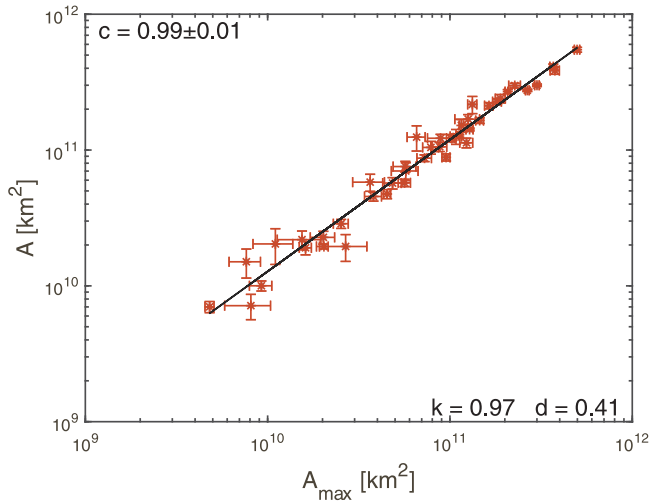


Figure 8. Maximum of the instantaneous dimming area A_{\max} against the cumulative dimming area A at the time t_{end} of the impulsive dimming evolution (in logarithmic space). The black line represents the linear regression fit to all data points. The correlation coefficient is given in the top left corner. The parameters of the linear regression performed in log–log space are given in the bottom right corner.

searched for their minimum in the time range of 6 hr after t_{start} . The mean dimming brightness parameters \bar{I}_{in} and \bar{I}_{cu} are derived from the same time steps as the corresponding total brightness. Figure 9 shows that the instantaneous and cumulative brightness extracted from LBR maps (the same is also true for BD data) are almost identical ($c = 0.99$, $k = 0.98$, $d = 0.10$). This means that we can use one approach to describe the dimming brightness for the comparative analysis.

In Table 1, we summarize all dimming parameters derived in our analysis. For each event, we list the STEREO satellite that was used for the analysis and the derived dimming properties: the maximum of the instantaneous dimming area A_{\max} , cumulative area A , maximal cumulative area growth rate \dot{A} , total dimming brightness from LBR data (cumulative $I_{\text{br,cu}}$ and instantaneous $I_{\text{br,in}}$), total dimming brightness from BD data (cumulative $I_{\text{bd,cu}}$ and instantaneous $I_{\text{bd,in}}$), mean instantaneous brightness $|\bar{I}_{\text{br,in}}|$, brightness change rate $\dot{I}_{\text{br,in}}$, and duration of the impulsive phase of the dimming t_{dur} . The CME quantities, such as the mass m_{CME} and the maximal speed v_{max} , are listed in the last columns of the table.

Figure 10 shows the distributions of the main dimming parameters derived from the whole data set: the cumulative dimming area A and its growth rate dA/dt , the absolute mean intensity from LBR data $\bar{I}_{\text{br,in}}$, and the duration of the impulsive phase t_{dur} (note that panels (a)–(c) are shown in the logarithmic scale). The dimming areas range from 7.0×10^9 to $5.5 \times 10^{11} \text{ km}^2$, with a mean value of $1.33 \pm 1.23 \times 10^{11} \text{ km}^2$. The area growth rate dA/dt varies from 2.7×10^6 to $2.9 \times 10^8 \text{ km}^2 \text{ s}^{-1}$, with a mean value of $7.41 \pm 6.96 \times 10^7 \text{ km}^2 \text{ s}^{-1}$. The mean brightness decrease of the total dimming regions varies in the interval $[-0.41, -0.18]$; the mean value is -0.28 ± 0.05 (note that values of brightness are calculated from LBR data). The duration of the impulsive dimming phase varies from 25 to 155 minutes. On average, it lasts for 66 ± 28 minutes.

In addition to the characteristic dimming parameters listed above, we estimated the recovery time of the dimmings, which indicates how fast the corona restructures and refills after the erupting CME. The recovery time t_{rec} is defined as the difference between the time of the maximal instantaneous area

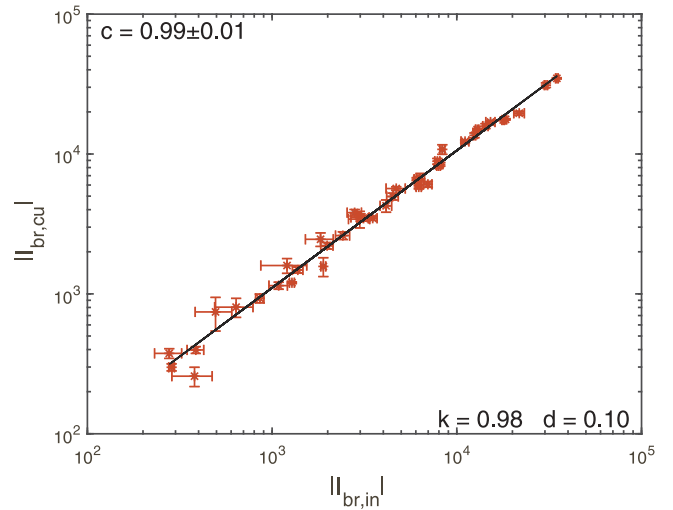


Figure 9. Absolute values of the cumulative total brightness $|I_{\text{br,cu}}|$ vs. absolute values of the instantaneous total brightness $|I_{\text{br,in}}|$ of the dimming regions, calculated from LBR maps. The black line represents the linear regression fit to all data points. The coefficients of the fitting line are presented in the bottom right corner. The corresponding correlation coefficient is given in the top left corner.

$A_{\text{in}}(t)$ ($=A_{\max}$) and the moment when the value of the instantaneous dimming area $A_{\text{in}}(t)$ falls below 50% of its maximum ($=0.5 \cdot A_{\max}$). For five events, it was impossible to calculate the recovery time because of subsequent CME eruptions from the same active region during the dimming recovery. The distribution of the parameter t_{rec} for the other 38 dimming events is plotted in Figure 11. The recovery time varies from 0.7 to 10.9 hr with a mean value of 4.6 ± 2.8 hr. However, for seven events of the sample, the derived recovery times are underestimated, as the drop to a value of $0.5 \cdot A_{\max}$ was not reached within the 12 hr length of the time series that we studied for each event. We note that this includes the two example events. The histogram seems to indicate a bimodal distribution with one group with fast recovery (less than ~ 6 hr) and another group with longer recovery times of >6 hr. To provide a definite conclusion on that, a larger sample would be needed, and one would need to follow the dimmings over a longer time range. The analysis of the dimming recovery time is important, as it provides information on the post-eruptive phase of the CME and the coronal restructuring.

4.2. Relation between Off-limb and On-disk Dimmings

We compare the dimming parameters that we obtained from the STEREO/EUVI 195 Å off-limb observations with the corresponding outcomes for the dimmings observed on-disk by SDO/AIA 211 Å in Dissauer et al. (2018b, 2019). Figure 12 shows the scatter plot between the dimming areas derived from on-disk and off-limb observations, which reveals a strong correlation ($c = 0.63 \pm 0.10$). For the events under study, off-limb dimmings tend to be larger than their corresponding on-disk counterparts; only eight events reveal a smaller dimming area for the off-limb observations compared to the on-disk areas.

In order to investigate whether the position of the STEREO satellites significantly affects the derived dimming area via projection effects or by obscuring parts of the dimming region behind the limb, we studied the dimming areas as a function of source region location with respect to the observing spacecraft.

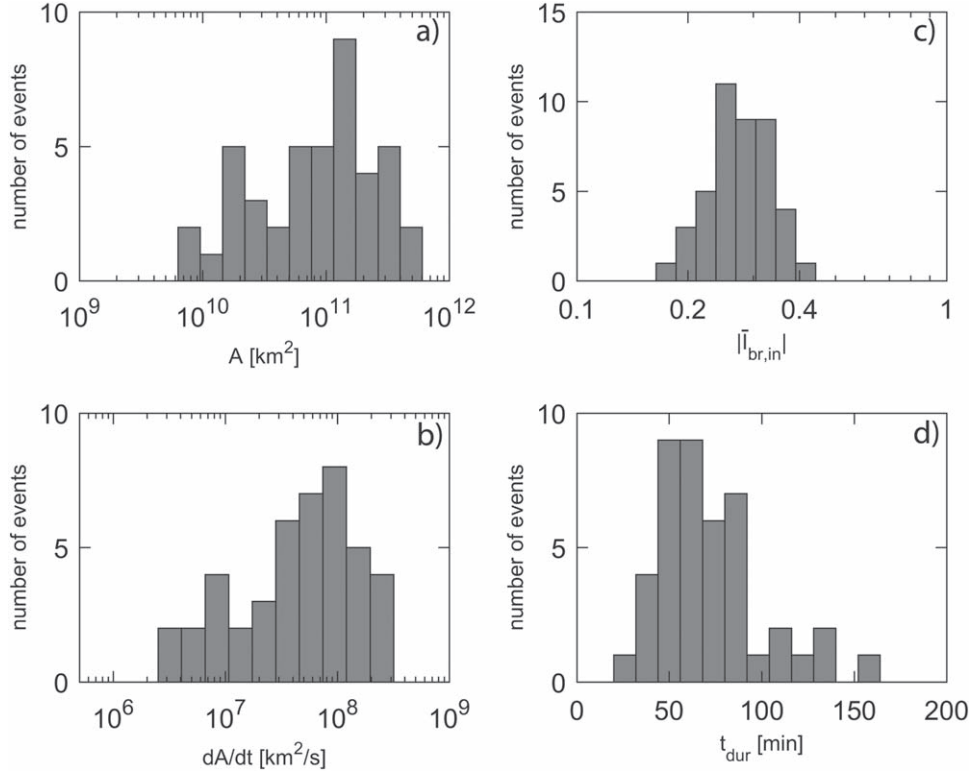


Figure 10. Distributions of characteristic dimming parameters: (a) maximum of the cumulative dimming area A , (b) maximum of the cumulative area growth rate dA/dt , (c) absolute values of the mean intensity from LBR data $|\bar{I}_{br,in}|$, and (d) duration of the dimming impulsive phase t_{dur} . Panels (a)–(c) are presented in logarithmic space and panel (d) in linear space.

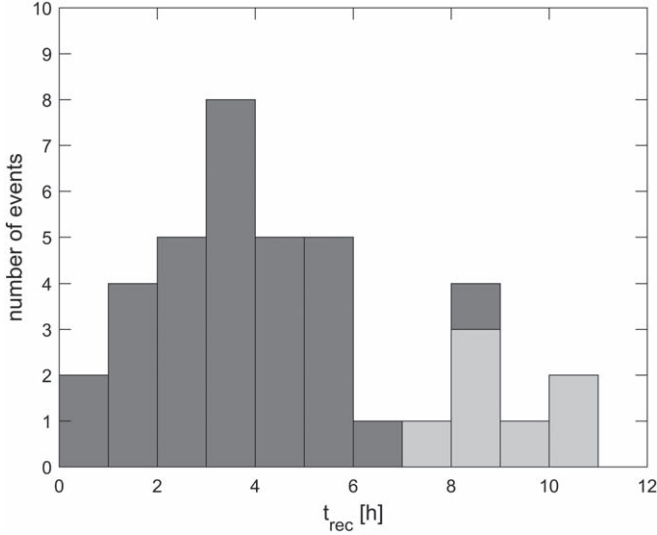


Figure 11. Distribution of dimming recovery times derived from 38 events of our sample. Note that for seven events (light colored bars), the derived recovery time gives only a lower estimate.

Figure 13 shows the ratio of the off-limb area $A_{off-limb}$ and on-disk area $A_{on-disk}$ against the central meridian distance (CMD) of the CME source region for the STEREO spacecraft. The coordinates of the dimming sources are derived from the heliographic positions of the associated flares given in Dissauer et al. (2018b). We can notice that all of the events were observed with a CMD in the range $[60^\circ, 130^\circ]$, but there is no significant dependence of the area ratio between the off-limb and on-disk observations on the CMD. Also, there is no

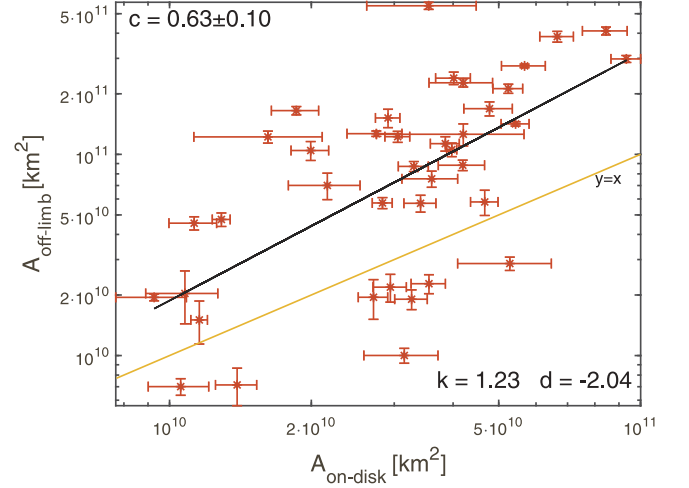


Figure 12. Scatter plot of the dimming areas derived off-limb by STEREO/EUVI, $A_{off-limb}$, and on-disk by SDO/AIA, $A_{on-disk}$, in logarithmic space. The black line represents the linear regression fit to all data points. The orange line shows the one-to-one relation. The corresponding correlation coefficient is given in the top left corner. The parameters of the linear regression performed in log–log space are given in the bottom right corner.

obvious change at a CMD of $>90^\circ$, i.e., for events where for STEREO the associated flare is located behind the limb, and thus part of the dimming regions may be obscured.

Figure 14 shows the scatter plot of total instantaneous brightness calculated from off-limb and on-disk observations by using LBR (top panel) and BD (bottom panel). The correlation coefficients result in $c = 0.60 \pm 0.14$ and 0.77 ± 0.09 , respectively. The regression lines (black) have a slope coefficient close

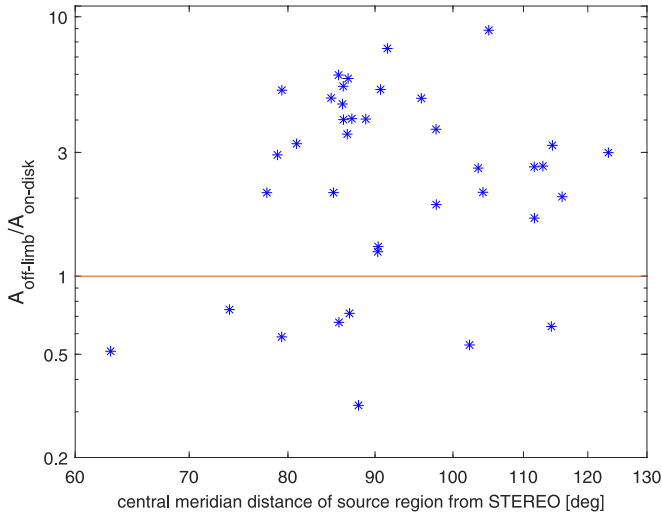


Figure 13. Ratio of the extracted off-limb and on-disk dimming areas vs. the CMD of the source region from the STEREO satellite. The orange line corresponds to a one-to-one relation.

to 1 ($k = 0.98$ and 1.06) and are therefore almost parallel to the 1:1 correspondence lines (orange), indicating that both parameters are linearly related.

4.3. Relation between Off-limb Dimming and CME Parameters

Figure 15 shows the cumulative off-limb dimming area A against the mass (top panel) and maximum speed (bottom panel) of the CME. We obtain a very high correlation between the dimming area and CME mass, $c = 0.82 \pm 0.06$ (in logarithmic space); i.e., the larger the area of the dimming, the more mass the associated CME contains. This correlation provides strong support for the physical interpretation of the appearance of the dimming as a density depletion due to the evacuation of plasma. These results are in agreement with the findings for the on-disk coronal dimmings by Dissauer et al. (2019), where $c = 0.69 \pm 0.10$. We also find a high correlation between the area of the dimming A and the speed of the CME ($c = 0.67 \pm 0.10$ in logarithmic space).

In addition, we also investigated the relation between the dynamic evolution of the dimming, as described by the peak of its area growth rate dA/dt , and the parameters of the associated CME (Figure 16). The correlation coefficients in logarithmic space are $c = 0.76 \pm 0.08$ and 0.59 ± 0.14 , respectively, indicating a close connection between the dimming growth rate with the mass and speed of the associated CME.

Figure 17 shows the correlation plots of the absolute values of total instantaneous dimming brightness calculated from LBR data against the CME mass and maximal speed (bottom). The correlation coefficients are $c = 0.75 \pm 0.08$ and 0.63 ± 0.11 , respectively, indicating a strong correlation. In addition, in Figure 18, we show the correlation between the mean instantaneous brightness $|\bar{I}_{br,in}|$ and the CME speed ($c = 0.48 \pm 0.14$).

We also obtained a strong correlation between the dimming brightness change rate and the maximal speed of the CME: the faster the total dimming brightness is changing, the higher the velocity of the associated CME. Figure 18 shows the absolute values of the instantaneous brightness change rate calculated from LBR data against the CME maximal speed. The correlation coefficient is $c = 0.61 \pm 0.12$.

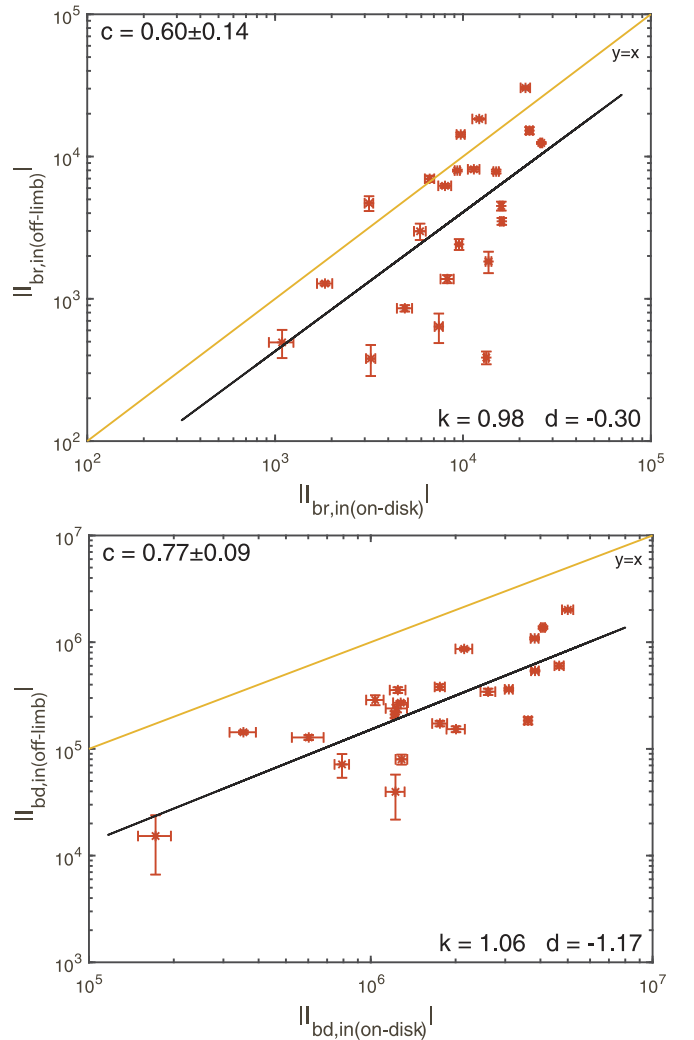


Figure 14. Comparison of the total instantaneous brightness from LBR (top panel) and BD (bottom panel) data for on-disk and off-limb observations, presented in absolute values. The black line represents the linear regression fit to all data points. The orange line shows the one-to-one relation. The corresponding correlation coefficients are given in the top left corner of each panel. The parameters of the linear regression performed in log-log space are given in the bottom right corner.

5. Summary and Discussion

We have developed a robust automated algorithm for the segmentation of coronal dimmings above the solar limb in STEREO/EUVI 195 Å images. The method is based on the combination of BD and LBR data using a region-growing algorithm. This segmentation algorithm was applied to 43 off-limb coronal dimming events, and characteristic parameters describing their dynamic evolution, size, and brightness were derived. The events under study occurred between 2010 May and 2012 September, when the two STEREO satellites were close to quadrature position with respect to the Sun–Earth line. This unique setting allows us to derive the properties of the coronal dimmings above the solar limb in the STEREO/EUVI data and, for the first time, to compare them with parameters of the same dimmings observed against the solar disk by SDO/AIA, as well as with the associated CME kinematics and mass derived above the limb (minimizing projection effects) in Dissauer et al. (2018b, 2019). This approach provides us with important insight into the different projections of the coronal

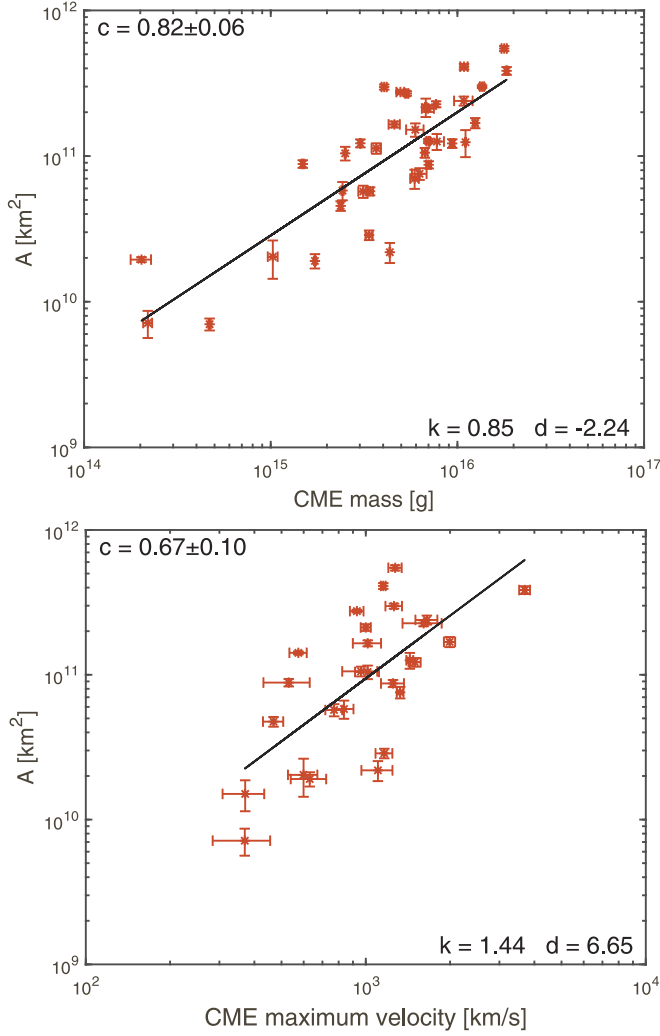


Figure 15. Cumulative area of the coronal dimming A against the CME mass m_{CME} (top) and maximal speed v_{max} in logarithmic space. The black line represents the linear regression fit to all data points. The corresponding correlation coefficient is given in the top left corner. The parameters of the linear regression performed in log–log space are given in the bottom right corner.

dimmings and how they relate to the associated CME properties.

The off-limb dimming observations give us a line-of-sight integration across the CME from a lateral perspective. Thus, they provide us with a good view of its lateral expansion, but the radial view is limited in height by the field of view of the EUVI imagers. The on-disk dimming observations are an integration of emission along the line of sight of the CME propagation and thus correspond to a projection of the cross section of the CME from a top view. However, they are affected by the “background” emission of the lower atmosphere layers, which makes it difficult to extract faint dimming regions and their effects higher up in the corona. On the other hand, on-disk dimmings provide us with the earliest insight into Earth-directed CMEs in observations from the Sun–Earth line, before the CME front reaches the field of view of white-light coronagraphs. Thus, comparing the properties of coronal dimmings observed simultaneously from different views in their on-disk/off-limb projections, as well as their relation to the CME velocity and mass, allows us to assess the potential of

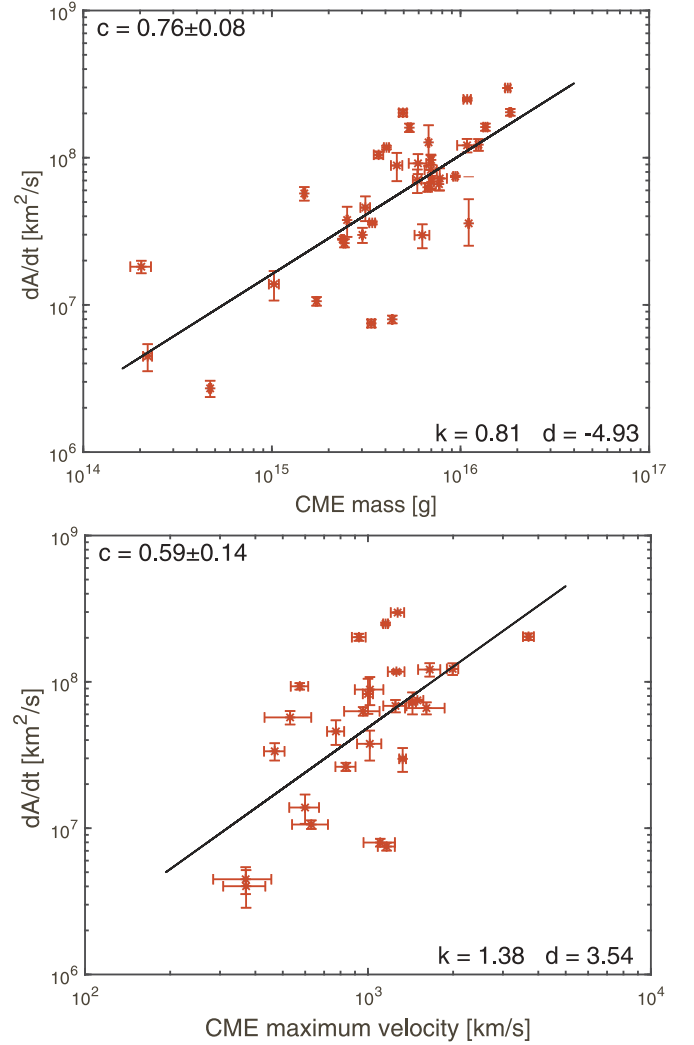


Figure 16. Correlation of the area growth rate dA/dt of the coronal dimming observed off-limb and the CME mass (top) and maximal speed (bottom). The black line represents the linear regression fit to all data points. The correlation coefficient is given in the top left corner of each panel. The parameters of the linear regression performed in log–log space are given in the bottom right corner of each panel.

using coronal dimmings for early CME characterization from satellites located either at L1 or L5.

Our main findings are as follows:

1. The derived off-limb dimming areas range from 7.01×10^9 to $5.48 \times 10^{11} \text{ km}^2$ (Figure 10). For the overlapping 39 events, which were also studied in Dissauer et al. (2018b, 2019), the mean value is $1.24 \pm 1.23 \times 10^{11} \text{ km}^2$, while the on-disk observations give $3.51 \pm 0.71 \times 10^{10} \text{ km}^2$. For eight events, the dimming area observed against the disk shows larger values than for the off-limb observations (see Figure 12), with a correlation coefficient of $c = 0.63 \pm 0.10$.
2. We compared the total dimming brightness calculated from LBR and BD data with the corresponding brightness extracted against the disk (Figure 14). The correlation coefficients are $c = 0.60 \pm 0.14$ and 0.77 ± 0.09 , respectively, and the slopes derived from the fits in logarithmic space are close to 1. This means that all of the decreases in the intensity of the dimming region observed on-disk and off-limb are linearly related to each other

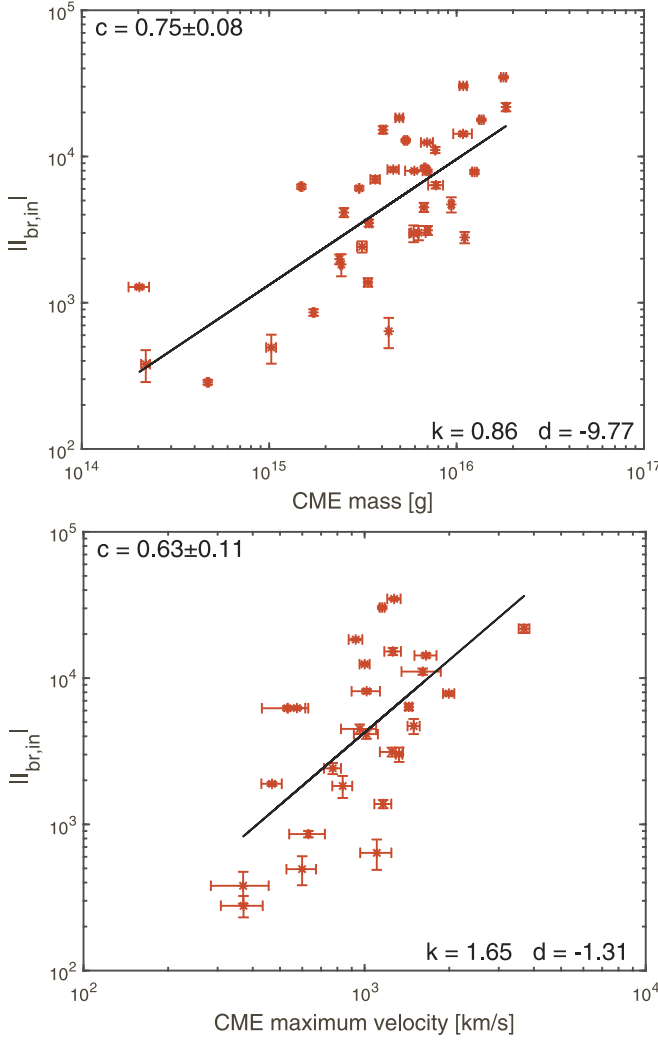


Figure 17. Absolute values of the total instantaneous dimming brightness $|I_{br,in}|$ against the mass (top panel) and maximum velocity (bottom panel) of the corresponding CME in logarithmic space. The brightness is calculated from LBR data. The black line represents the linear regression fit to all data points. The correlation coefficients are given in the top left corner of each panel. The parameters of the linear regression performed in log-log space are given in the bottom right corner of each panel.

(with respect to the logarithmic space), but in most cases, the on-disk dimming intensity is smaller (darker).

3. We also checked the duration of the impulsive dimming phase of 43 events obtained from off-limb observations (see panel (d) in Figure 10). Although the time cadence of the STEREO data is much lower than the cadence of SDO/AIA, the duration parameter for both on-disk and off-limb observations is, on average, ~ 60 – 70 minutes.
4. The dimming recovery time t_{rec} varies from 0.7 to 10.9 hr (Figure 11). The mean value is 4.6 ± 2.8 hr, which supports the results by Reinard & Biesecker (2008), where the mean of the recovery time 4.8 ± 0.3 hr was reported, as well as with Krista & Reinard (2017), who found that the time from the area maximum to when dimming fully disappears is, on average, ~ 6 hr.
5. The CME mass shows the strongest correlation with the parameters, reflecting the total extent of the dimming, i.e., its area and total brightness: $c = 0.82 \pm 0.06$ and 0.75 ± 0.08 , respectively (see Figures 15 and 17). This

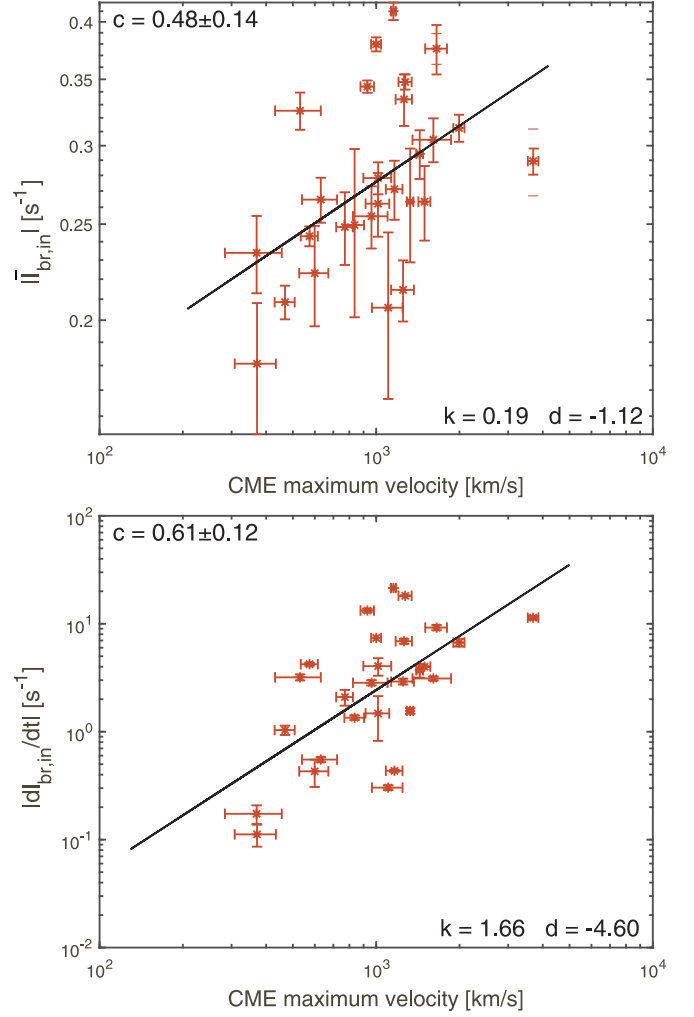


Figure 18. Mean instantaneous dimming brightness $\bar{I}_{br,in}$ (top panel) and instantaneous brightness change rate $|dI_{br,in}/dt|$ (bottom panel), calculated from LBR maps, against the maximum velocity of the associated CME in logarithmic space. All parameters are presented by their absolute values. The black line represents the linear regression fit to all data points. The correlation coefficients are given in the top left corner of each panel. The parameters of the linear regression performed in log-log space are given in the bottom right corner of each panel.

result demonstrates that off-limb observations are able to provide a more accurate estimation of the CME mass.

6. The maximal CME speed correlates with the parameters describing the dynamics of the coronal dimmings: $c = 0.59 \pm 0.14$ for the correlation with the area growth rate dA/dt (see Figure 16) and $c = 0.61 \pm 0.12$ for the correlation with the instantaneous brightness change rate derived from LBR data (Figure 18). In addition, there is also a moderate correlation ($c = 0.48 \pm 0.14$) of the CME maximal velocity and the mean brightness of the dimming (see also Figure 18).

Figure 12 shows that for the events under study, off-limb dimmings tend to be larger than their corresponding on-disk counterparts. Due to the line-of-sight integration, the density depletion higher up in the corona may not be detected for on-disk observations due to brighter lower-lying regions. Base ratio images, showing relative changes in intensity, allow us to detect these regions from the off-limb perspective. At the same time, the area parameters show a strong correlation ($c \sim 0.63$),

which may indicate that mostly large dimmings are also detected in the higher corona.

Although the area of the dimming observed off-limb is typically larger than that on-disk, the absolute total brightness obtained from off-limb BD data is lower than the one obtained from the on-disk data (see Figure 14). Dimming regions detected higher up in the corona show less significant intensity decreases compared to dimming regions detected close to the surface, where the density of the corona is higher. The biggest area contribution of dimming regions detected off-limb results from these regions higher up, but they do not contribute much to the overall intensity decrease of the dimming region.

We found a very strong correlation between the CME mass and the dimming area, which confirms the relation of coronal dimmings and CME physical properties for the off-limb viewpoint. This is similar to the previous findings from the on-disk study (Dissauer et al. 2019). More massive CMEs evacuate more plasma and create larger regions of EUV density depletion, which we detect from different lines of sight (see Figure 15). The correlation coefficient revealed an even higher value than for on-disk results ($c = 0.82 \pm 0.06$ for off-limb against $c = 0.69 \pm 0.10$ for on-disk). This may be related to the fact that the CME parameters were also extracted from STEREO data. Thus, the projection effects may cause similar uncertainties for the dimming quantities and the CME parameters derived.

The maximal area of the dimming also demonstrates a high correlation coefficient with the speed of the CME ($c = 0.67 \pm 0.10$ in logarithmic scale). This relationship supports the finding that faster CMEs are usually also more massive (Aschwanden 2016; Mason et al. 2016; Dissauer et al. 2019) and therefore also associated with a larger coronal dimming region. The correlation of the area growth rate with the CME speed and mass ($c \sim 0.6$ – 0.7) supports this statement (Figure 16).

According to Mason et al. (2016), CMEs that are associated with dark and large dimmings tend to be more massive. The analysis of the dimmings on-disk by Dissauer et al. (2019) supports this statement; the correlation coefficient is $c \sim 0.6$ for the correlation between the dimming total brightness and the CME mass. In the off-limb case, the total dimming brightness $|I_{\text{br,in}}|$ reveals an even stronger correlation with the CME mass ($c \sim 0.75$). Thus, dimmings can provide a measure of the amount of plasma evacuation in the CME; darker dimmings indicate a larger density depletion.

Furthermore, we found a moderate correlation ($c = 0.48 \pm 0.14$) of the mean instantaneous brightness $|\bar{I}_{\text{br,in}}|$ with the CME speed (Figure 18). As the coronal plasma density strongly decreases with height, this correlation may indicate that faster CMEs tend to develop lower in the corona. This is consistent with studies of the CME source region characteristics and the fact that low in the corona, the magnetic field and thus the driving Lorentz force is stronger (Vršnak et al. 2007; Bein et al. 2011). The same correlation from the on-disk observations reveals $c = 0.68 \pm 0.08$.

The dimming recovery times are suggestive of a bimodal distribution, with one group of t_{rec} values smaller than 6 hr and another group with values of $t_{\text{rec}} > 6$ hr. This may indicate that there exist two different classes of dimmings as concerns the replenishment properties of the corona in the aftermath of a CME eruption. We also note that for seven events in our sample, the recovery time defined by the decrease of the instantaneous dimming area to 50% of its peak value was not

reached within the studied time range of 12 hr and may thus be even longer. These findings can be set in context with the detailed case studies of the plasma properties of several coronal dimming events using DEM analysis in Vanninathan et al. (2018). These authors found that in the localized core dimming regions, the density drops sharply within about 30 minutes and stays at these low levels for >10 hr, whereas in the secondary dimming regions, the density drop is more gradual, and the corona starts with the recovery and replenishment within 1–2 hr. This finding was interpreted as evidence that the core dimmings are a signature of a flux rope still connected to the Sun, thus preventing the refill of coronal plasma in these regions. Further studies are needed and planned to obtain a better picture of the processes of coronal replenishment and recovery in the wake of a CME, as is most prominently evidenced by the evolution of its dimming properties.

6. Conclusion

We performed a statistical analysis of 43 coronal dimming events that occurred during the time range between 2010 May and 2012 September that were observed simultaneously on-disk by SDO and off-limb by the STEREO satellites. The unique location of these satellites allowed us for the first time to look into the connection of the coronal dimmings and their associated Earth-directed CMEs statistically and compare the results obtained from multiple-viewpoint observations. Based on regression analysis, we also confirm the relation of on-disk coronal dimmings and CME parameters presented in Dissauer et al. (2019) for the off-limb viewpoint for certain parameters providing even higher correlation coefficients than with the reported dimmings observed from on-disk by SDO/AIA. Parameters describing the total dimming extent, i.e., area and total brightness, strongly correlate with the CME mass ($c \sim 0.7$ – 0.8). The derivative of these parameters, i.e., the area growth rate and brightness change rate, show a high correlation with the CME speed ($c \sim 0.6$), indicating the close relation between the CME and dimming dynamics.


In our chosen observation range (2010 May–2012 September), the STEREO-A and -B satellites were located close to an L5/L4 configuration. The results from our study, therefore, also have relevant implications for the planned future L5 space weather mission, where Earth-directed CMEs, which are the most geoeffective, will be observed off-limb. The observations of coronal dimmings by solar EUV imagers may help us to obtain a better characterization of Earth-directed CMEs, which is relevant for space weather applications. The distinct statistical relations derived between dimming parameters and decisive CME quantities for the different scenarios of L1 and L5 satellite locations (with correlation coefficients up to 0.8) provide a profound basis for improving early calculations of the speed and mass of Earth-directed CMEs by also including the information on coronal dimmings.

The authors thank the referee for constructive and helpful comments that improved the manuscript. K.D. and A.M.V. acknowledge funding by the Austrian Space Applications Programme of the Austrian Research Promotion Agency FFG, BMVIT projects ASAP-11 4900217 and ASAP-14 865972, as well as Austrian Science Fund (FWF) projects P24092-N16 and P27292-N20. The STEREO/SECCHI data are produced by an international consortium of the Naval Research Laboratory (USA), Lockheed Martin Solar and Astrophysics

Lab (USA), NASA Goddard Space Flight Center (USA), Rutherford Appleton Laboratory (UK), the University of Birmingham (UK), Max-Planck-Institut für Sonnenforschung (Germany), Centre Spatiale de Liège (Belgium), Institut d'Optique Théorique et Appliquée (France), and Institut d'Astrophysique Spatiale (France).

ORCID iDs

Galina Chikunova  <https://orcid.org/0000-0002-1317-0020>

Karin Dissauer  <https://orcid.org/0000-0001-5661-9759>

Tatiana Podladchikova  <https://orcid.org/0000-0002-9189-1579>

Astrid M. Veronig  <https://orcid.org/0000-0003-2073-002X>

References

- Aschwanden, M. J. 2016, *ApJ*, **831**, 105
- Aschwanden, M. J., Wuelser, J. P., Nitta, N. V., & Lemen, J. R. 2009, *SoPh*, **256**, 3
- Attrill, G., & Wills-Davey, M. 2009, *SoPh*, **262**, 461
- Bein, B., Berkebile-Stoiser, S., Veronig, A., et al. 2011, *ApJ*, **738**, 191
- Bewsher, D., Harrison, R., & Brown, D. S. 2008, *A&A*, **478**, 897
- Burkepile, J., Hundhausen, A., Stanger, A., Cyr, O., St., & Seiden, J. 2004, *JGRA*, **109**, A03103
- Dissauer, K., Temmer, M., Veronig, A. M., Vanninathan, K., & Magdalenic, J. 2016, *ApJ*, **830**, 92
- Dissauer, K., Veronig, A. M., Temmer, M., & Podladchikova, T. 2019, *ApJ*, **874**, 123
- Dissauer, K., Veronig, A. M., Temmer, M., Podladchikova, T., & Vanninathan, K. 2018a, *ApJ*, **855**, 137
- Dissauer, K., Veronig, A. M., Temmer, M., Podladchikova, T., & Vanninathan, K. 2018b, *ApJ*, **863**, 169
- Gopalswamy, N., Yashiro, S., Michalek, G., et al. 2009, *EM&P*, **104**, 295
- Gosling, J. T. 1993, *JGR*, **98**, 18937
- Harra, L. K., & Sterling, A. C. 2001, *ApJL*, **561**, L215
- Harrison, R., & Lyons, M. 2000, *A&A*, **358**, 1097
- Hudson, H. S., Acton, L. W., & Freeland, S. L. 1996, *ApJ*, **470**, 629
- Kaiser, M. L., Kucera, T. A., Davila, J. M., et al. 2008, *SSRv*, **136**, 5
- Kazachenko, M. D., Lynch, B. J., Welsch, B. T., & Sun, X. 2017, *ApJ*, **845**, 49
- Knipp, D. J., Fraser, B. J., Shea, M., & Smart, D. 2018, *SpWea*, **16**, 1635
- Kraaikamp, E., & Verbeeck, C. 2015, *JWSC*, **5**, A18
- Krista, L. D., & Reinard, A. 2012, *ApJ*, **762**, 91
- Krista, L. D., & Reinard, A. A. 2017, *ApJ*, **839**, 50
- Lanzerotti, L. J. 2017, *SSRv*, **212**, 1253
- Lemen, J. R., Title, A. M., Akin, D. J., et al. 2012, *SoPh*, **275**, 17
- López, F. M., Cremades, M. H., Nuevo, F. A., Balmaceda, L. A., & Vásquez, A. M. 2017, *SoPh*, **292**, 6
- Mason, J. P., Woods, T. N., Webb, D. F., et al. 2016, *ApJ*, **830**, 20
- Podladchikova, O., & Berghmans, D. 2005, *SoPh*, **228**, 265
- Podladchikova, T., Veronig, A. M., Dissauer, K., Temmer, M., & Podladchikova, O. 2019, *ApJ*, **877**, 68
- Reinard, A., & Biesecker, D. 2008, *ApJ*, **674**, 576
- Rouillard, A. 2011, *JASTP*, **73**, 1201
- Sterling, A. C., & Hudson, H. S. 1997, *ApJL*, **491**, L55
- Thernisien, A., Vourlidis, A., & Howard, R. 2011, *JASTP*, **73**, 1156
- Thompson, B. J., Plunkett, S. P., Gurman, J. B., et al. 1998, *GeoRL*, **25**, 2465
- Tian, H., McIntosh, S. W., Xia, L., He, J., & Wang, X. 2012, *ApJ*, **748**, 106
- Vanninathan, K., Veronig, A. M., Dissauer, K., & Temmer, M. 2018, *ApJ*, **857**, 62
- Veronig, A. M., Gömöry, P., Dissauer, K., Temmer, M., & Vanninathan, K. 2019, *ApJ*, **879**, 85
- Veronig, A. M., Podladchikova, T., Dissauer, K., et al. 2018, *ApJ*, **868**, 107
- Vršnak, B., Maričić, D., Stanger, A. L., et al. 2007, *SoPh*, **241**, 85
- Wall, J. V., & Jenkins, C. R. 2012, *Practical Statistics for Astronomers* (Cambridge: Cambridge Univ. Press)
- Webb, D. F., & Howard, T. A. 2012, *LRSP*, **9**, 3
- Webb, D. F., Lepping, R. P., Burlaga, L. F., et al. 2000, *JGR*, **105**, 27251
- Wuelser, J.-P., Lemen, J. R., Tarbell, T. D., et al. 2004, *Proc. SPIE*, **5171**, 111
- Zarro, D. M., Sterling, A. C., Thompson, B. J., Hudson, H. S., & Nitta, N. 1999, *ApJL*, **520**, L139